

Transient dynamic distributed strain sensing using photonic crystal waveguides

HOSANGADI PRUTVI SAGAR,^{1,2} VIGNESH MAHALINGAM,¹ DEBIPROSAD ROY MAHAPATRA,^{1,*} GOPALKRISHNA HEGDE,³ SATHYANARAYANA HANAGUD,⁴ AND MOHAMMAD RIZWANUR RAHMAN²

¹Department of Aerospace Engineering, Indian Institute of Science, Bangalore 560012, India

²Department of Metallurgical and Materials Engineering, National Institute of Technology-Karnataka, Surathkal, Mangalore 575085, Karnataka, India

³Centre for Nano Science and Engineering, Indian Institute of Science, Bengaluru 560012, India

⁴School of Aerospace Engineering, Georgia Institute of Technology, Atlanta, Georgia 30332, USA

*Corresponding author: droymahapatra@aero.iisc.ernet.in

Received 10 July 2017; revised 1 September 2017; accepted 1 September 2017; posted 6 September 2017 (Doc. ID 302142); published 27 September 2017

This paper presents a new type of one-dimensional photonic crystal (PC) waveguide sensor and a technique for prediction of transient strain response accurately. The PC waveguide is integrated on a silicon substrate. We investigate the effect of non-uniform strain localization on the optical signal and use that information to capture the transient strain. Wavelength shift due to distributed strain field is modeled by incorporating the mechanically deformed geometry and photo-acoustic coupling through Pockels effect in a finite element formulation. We demonstrate the advantages of using our proposed method, where multiple spectral peak shift is used instead of single peak shift in order to improve sensing output accuracy and also to estimate the sensor parameter regressively, where the signal's bandwidth is limited. The maximum sensitivity of the waveguide sensor in terms of wavelength shift is estimated to be 0.36 pm/ μ strain in single-peak-based sensing, whereas the proposed adaptive multispectral estimation scheme shows an enhanced sensitivity of 4.029 pm/ μ strain. © 2017 Optical Society of America

OCIS codes: (050.5298) Photonic crystals; (050.1755) Computational electromagnetic methods; (130.3120) Integrated optics devices; (130.5296) Photonic crystal waveguides; (130.6010) Sensors.

<https://doi.org/10.1364/AO.56.007877>

1. INTRODUCTION

Dynamic distributed strain sensing is important in structural dynamics, vibration, shock measurement, and structural health monitoring. Electrical-resistance-based strain gauges and fiber optic sensors are widely used for strain sensing. Among these, fiber Bragg grating (FBG) sensors [1] have attracted much attention due to their great advantages, such as high accuracy and fast responsivity in measuring dynamic strain and the capability of multiplexing signals from several FBGs in a single fiber [2–4]. These sensors have the advantage of an easy implantation in fiber reinforced polymer composites [5], printed electronics, and in flexible electronic devices and structures [6]. Easy integration on host material or structural components makes them appropriate for distributed sensing [7]. Studies on transient strain sensing on a cantilever using piezoelectric piezoelectric polyvinylidene fluoride (PVDF) sensors [8–10] have been reported. They compete with FBGs and photonic crystal (PC) sensors. The transient dynamic changes in shape, strain, and temperature are the main concerns in sensor design, calibration, and deployment. Currently, optical sensors are used for sensing

various parameters in aerospace and marine vehicles, composite infrastructure, ground testing of vibration, and thermal loads. Embedding the sensors into composite material and multiplexing several point-wise measurements through Bragg grating, polarizing elements, etc., are important aspects in the above applications. Point-wise sensing in a contact or non-contact mode increases the complexity of tuning time-resolved spatial response, such as transient dynamic strain, shock, and temperature spikes. The electrical-resistance-based strain sensors require electrical wires and interconnects. Here, the sensor performance is limited by its size and its dynamic resonance. Micro-electro-mechanical systems (MEMS) sensors having smaller size and higher sensitivity still require electrical circuit, packaging, and interconnects which, becomes challenging.

In order to reduce some of the above complexities, and to realize higher density of sensing through chip integrated sensor arrays, optical resonators with wide dynamic characteristics are proposed [11]. PCs are periodic nanostructures with the refractive index modulated at a wavelength of light. One-dimensional (1D) PCs or photonic bandgap structures in high refractive

index contrast media are one-dimensional periodic layers of optical waveguides, where a photonic bandgap is created. This can be used in sensing applications. They are novel candidates for integrated optoelectronic applications due to their strong confinement of optical modes and wider bandgap properties, which can be tuned or controlled by various different external stimuli like vibration, electromagnetic polarization, chemical effect, etc. Distributed Bragg reflectors based on the principle of 1D PC are attractive wavelength selective devices [12].

Distributed Bragg reflectors etched on either the top or sidewalls of integrated optical waveguides are widely used as wavelength division multiplexing filters [13], bio-mechanical sensors [14], and lasers [15]. The 1D PCs with waveguide width and periodicity in the micrometer or sub-micrometer regime can be fabricated with UV lithography followed by a wet or dry etch of the exposed area [16].

In this paper, we consider a deeply etched integrated 1D PC design with silicon strip waveguides over a longitudinal-bending deformation type structure for its optical response under dynamic mechanical strain, vibration, and shock wave sensing, including the effect of non-uniform strain localization and transients. The effect of dynamic localization of strain field in PCs, where the size of the PCs is larger than the length scale of strain localization, is examined. This aspect is poorly understood in the literature.

We first establish a correlation between strain and wavelength shift in static longitudinal loading for a single spectral peak. Next, the correlation between strain and wavelength in static transverse loading is established. Finally, the strain in longitudinal loading is correlated to multiple spectral peak shifts, and a method to use these characteristics by minimizing the error in dynamic strain sensing is explained. Experimental data from a hypersonic shock tube experiment is used in illustrating dynamic strain sensing.

2. SIMULATION MODEL

A. Electromagnetic Analysis

Figure 1 shows a schematic view of the 1D PC waveguide on the substrate. The guiding medium is silicon with a refractive index of 3.5. The etch depth or vertical height of the PC strips are assumed to be significantly large so that the effective refractive index of the mode of light propagation remains unchanged when considered along with the substrate. In such a design, the incident light and the reflected/transmitted light from the PC can be guided via the extended waveguides at both ends (see Fig. 1). A mechanical force is applied over the YZ cross section at the far end of the structure on the output side of the waveguide.

The 3D geometry, shown in Fig. 1(a), is reduced to an equivalent 2D model with the grating part [see Fig. 1(b)]. Two possible configurations—plane view (XY) and longitudinal cross section (XZ)—of the 3D structure are analyzed. The longitudinal configuration accounts for the complete depth profile of the grating and the underlying substrate, and is used for the electromagnetic field and strain modeling.

The 1D PC, as shown in Fig. 1, is designed according to the Bragg's condition for reflection [17,18]:

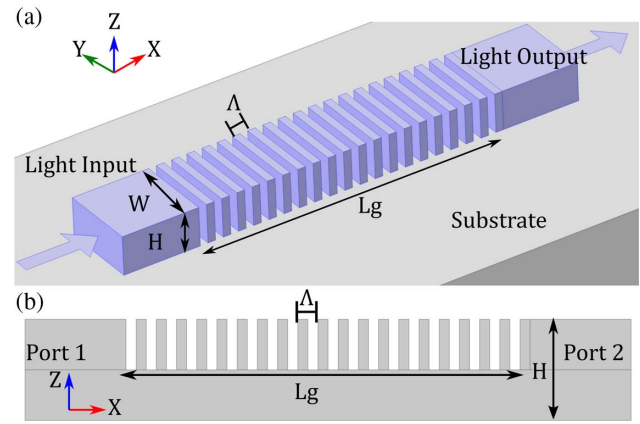


Fig. 1. (a) Schematic of 1D PC integrated on the substrate and (b) 2D profile view of the waveguide used in FEM analysis. The structure consists of a waveguide ($W = 8 \mu\text{m}$, $H = 5 \mu\text{m}$, $\Lambda = 2 \mu\text{m}$, $Lg = 40 \mu\text{m}$).

$$m\lambda_B = 2(n_a d_a + n_b d_b), \quad (1)$$

where λ_B is the Bragg wavelength and $n_i d_i$ is the optical path length of i th layer with refractive index n_i and geometric path length d_i . In the present model, periodic layers are of air/Si, so that $n_a = n_{\text{air}}$ and $n_b = n_{\text{Si}}$, and the corresponding thicknesses of these layers are d_a and d_b . For $d_a = d_b = d = 1 \mu\text{m}$, Eq. (1) gives a peak reflection wavelength of λ_B of $1.5 \mu\text{m}$ for a period (Λ) = $2 \mu\text{m}$ and grating order $m = 6$.

For the 1D PC to have complete bandgap, the height in the z direction (vertical etch) has to be ideally large. Practically, this is nearly achieved by making the etch depth much larger than wavelengths [17,18]. We consider the etch depth as $5 \mu\text{m}$ ($>2\Lambda$ approximately). This will ensure that a significant fraction of the power will be coupled to the PC from the input port side. The cantilever beam has 1:3 width to length ratio and a thickness of $200 \mu\text{m}$.

To evaluate the behavior of the PC, we perform finite element (FE) simulations. Analysis is done in two steps: first, the transmission characteristics of the undeformed PC are analyzed; second, the coupled effect of deformation of the substrate on the optical response under static and dynamic loading are studied. The nature of shift in the optical transmission characteristics is used to develop a sensor calibration procedure.

The electromagnetic wave propagation characteristics are analyzed using the frequency domain finite element model. Here, the frequency domain version of the wave propagation equation is written as

$$\nabla \times \left(\frac{1}{\mu_r} \nabla \times E \right) - k_0^2 \epsilon_r E = -jk_0 Z_0 J, \quad (2)$$

where $E(X, t) = \tilde{E}(X, t) \exp(j\omega t) = \hat{E}(\omega) \exp(jk_0 X + j\omega t)$ and $\epsilon_r = (n - ik)^2$ is the complex dielectric permittivity, given by the refractive index " n " of the material and loss factor κ , k_0 is the free-space wavenumber given by $k_0 = 2\pi/\lambda_0$, ω is the angular frequency, and J is the current density. In this study, we take $\mu_r = 1$. We use the weak integral form of Eq. (2) in the variational formulation of FE [19] as

$$F(\mathbf{E}) = \int_{\Omega} \left[\frac{1}{\mu_r} |\nabla \times \mathbf{E}|^2 - k_0^2 \epsilon_r |\mathbf{E}|^2 \right] d\Omega + jk_0 Z_0 \int_{\Omega} \mathbf{E} \cdot \mathbf{J} d\Omega, \quad (3)$$

where Z_0 is the impedance considered as 50Ω . FE formulation results in variational minimization of the functional $F(\mathbf{E})$ in Eq. (3), which is implemented in COMSOL Multiphysics software [20].

The time average of the frequency domain spectral power (P) at the ports is calculated. The scattering coefficients are determined as $S_{11} = (P_{R1}/P_{I1})^{1/2}$ and $S_{21} = (P_{T2}/P_{I1})^{1/2}$, where I , R , and T are incident, reflected, and transmitted quantities, respectively, at the input port 1 and output port 2.

Although the bottom part of the Si substrate would contribute to some amount of transmission, we want to maximize the light coupled to the deeply etched grating part. FE simulations are useful to develop the necessary understanding. However, the electromagnetic and strain field distributions are not straightforward to simulate together. It is also important to evaluate how the preliminary design for λ_B is working in a more realistic condition of field localization and that we are interested in correlating the spatial information to the multiple spectral peaks.

To obtain the strain field distribution in the waveguide, we assume a linear elastic model in 2D (plane stress) of the domain including stress transfer from the host substrate [see Fig. 1(a)]. The governing equation for the elastodynamic problem is expressed as

$$\rho \frac{\partial^2 \mathbf{u}}{\partial t^2} = \nabla \cdot \boldsymbol{\sigma} + \mathbf{f}_v, \quad (4)$$

where $\boldsymbol{\sigma}$ is the stress tensor, \mathbf{f}_v is the applied body force, and \mathbf{u} is the displacement vector.

The detailed view of the simulation setting is given in Section 4. The following material properties are used: steel as the substrate with Young's modulus $E = 205$ GPa, density $\rho = 7850 \text{ kgm}^{-3}$, and Poisson ratio $\nu = 0.28$. The displacement degrees of freedom at the left end of the cantilever is fully restrained as a fixed end boundary condition. Forces are applied to the free end of the cantilever, first longitudinally and then transversely, to analyze the in-plane and bending strain, respectively.

An important feature in the present waveguide is that the air layer thickness changes due to the displacement of the adjacent Si layers. This change in the air layer thickness along the mid-depth section of the grating is estimated and incorporated in electromagnetic simulations of the deformed grating to find the shift in transmission peak wavelengths. Additionally, the effect of change in the dielectric medium due to distributed strain is included by mapping the simulated strain field and computing the dielectric tensor at each material point in electromagnetic simulation. Finally, time-dependent simulation results are analyzed in terms of sensor output by employing a time-dependent excitation, which is obtained from a shock wave experiment. All the cases of static and dynamic loading are explained in detail in Section 4. The range of loads are chosen in such a way that the maximum stress in the structure in any case at any point of time is below the yield stress of

silicon, considering anisotropically etched sharp cornered features [21].

B. Deformation Coupled Optical Transport

We consider the standard silicon wafer having a top surface parallel to the [001] plane. Material constitutive relation in 45° rotated frame of reference is considered for the etched grating and can be expressed as

$$\sigma_{ij} = C_{ijkl} \epsilon_{kl}, \quad (5)$$

where σ_{ij} is the stress tensor, C_{ijkl} is the elasticity tensor, and ϵ_{kl} is the strain tensor. After applying symmetry properties, the elasticity matrix considered in our simulation has the form in the [100] system of reference as

$$C_{ijkl} = \begin{bmatrix} 194.5 & 35.7 & 64.1 & 0 & 0 & 0 \\ 35.7 & 194.5 & 64.1 & 0 & 0 & 0 \\ 64.1 & 64.1 & 165.7 & 0 & 0 & 0 \\ 0 & 0 & 0 & 79.6 & 0 & 0 \\ 0 & 0 & 0 & 0 & 79.6 & 0 \\ 0 & 0 & 0 & 0 & 0 & 79.6 \end{bmatrix}, \quad (6)$$

with the values shown in GPa [20].

The electric displacement \mathbf{D} , dielectric tensor ϵ , electric field \mathbf{E} , and induced strain ϵ_{kl} are governed by the constitutive law [22–24]:

$$\mathbf{E} = \epsilon^{-1} \mathbf{D}, \quad (7)$$

$$\epsilon^{-1} = \epsilon^{-1} + \Delta \epsilon^{-1}(\epsilon), \quad (8)$$

where $\Delta \epsilon^{-1}(\epsilon)$ is the strain-induced change in the inverse dielectric tensor. The orthotropic dielectric property of the unstrained Si is given by

$$\epsilon = \begin{bmatrix} 11.68 & 0 & 0 \\ 0 & 11.68 & 0 \\ 0 & 0 & 11.68 \end{bmatrix}, \quad (9)$$

The strain-induced change in the inverse dielectric tensor is given by [22–24]

$$\Delta \epsilon^{-1}(\epsilon) = P_{ijkl} \epsilon_{kl}, \quad (10)$$

where P is the photo-elastic tensor. Electrostriction-induced strain components are neglected, since it is a second-order effect as the electric field intensity is very small. The photo-elastic tensor P is given as

$$P = \begin{bmatrix} P_{11} & P_{12} & P_{12} & 0 & 0 & 0 \\ P_{12} & P_{11} & P_{12} & 0 & 0 & 0 \\ P_{12} & P_{12} & P_{11} & 0 & 0 & 0 \\ 0 & 0 & 0 & P_{44} & 0 & 0 \\ 0 & 0 & 0 & 0 & P_{44} & 0 \\ 0 & 0 & 0 & 0 & 0 & P_{44} \end{bmatrix}, \quad (11)$$

where $P_{11} = -0.094$, $P_{12} = 0.017$, and $P_{44} = -0.051$ for silicon [23] considering {100} as the x -coordinate axis. Using the fourth-order transformation matrix [24], this photo-elastic tensor is rotated by 45° . The rotated photo-elastic tensor $P^{(45^\circ)}$ is finally obtained as

$$P^{(45^\circ)} = \begin{bmatrix} -2.3012 & -0.1990 & 0.0935 & 0 & 0 & -0.4995 \\ -0.1990 & -0.0512 & 0.0170 & 0 & 0 & 0 \\ 0.035 & 0.0170 & -0.0940 & 0 & 0 & 0 \\ 0 & 0 & 0 & -0.0510 & 0 & 0 \\ 0 & 0 & 0 & 0 & -0.0510 & 0 \\ 0.4995 & 0 & 0 & 0 & 0 & -0.2220 \end{bmatrix}, \quad (12)$$

which is incorporated in the strain-dependent dielectric property. This scheme allows a realistic coupling of the deformation of the grating and the electromagnetism due to change in both the grating geometry as well as the material property. FE mesh convergence analysis is carried out to ensure that the results obtained are accurate. Convergence of the average strain distribution at the waveguide–substrate interface and at the base of the grating is achieved for an element size of $0.8 \mu\text{m}$ or smaller and it requires about 90,000 elements in the mesh [see Fig. 2(a)]. In the case of the electromagnetics simulation, the power spectral density (PSD), defined as

$$\text{PSD} = \frac{\int_{\lambda_{\min}}^{\lambda_{\max}} |S_{21}|^2}{\lambda_{\max} - \lambda_{\min}}, \quad (13)$$

is used to analyze the convergence of FE results [see Fig. 2(b)]. Convergence in the PSD is achieved for an element size of $0.1 \mu\text{m}$ or smaller and it requires about 1,00,000 elements. Hence, all further simulations were carried out with maximum size of the element as $0.08 \mu\text{m}$ with a uniformly dense mesh of 2,00,000 elements.

3. RESULTS AND DISCUSSION

Based on idealized calculations with Eq. (1), we estimated the PC structure to have a reflection band centered at 1480 nm . Each period consists of layers of $1 \mu\text{m}$ Si and $1 \mu\text{m}$ air. Twenty such bi-layers are present, giving a total grating length of $40 \mu\text{m}$. Owing to the high-index contrast between the periodic refractive indices, the structure has a very wide photonic bandgap of 165 nm ranging from 1401 nm to 1566 nm , as shown in Fig. 3.

Periodic peaks in the transmission spectra are observed between 1320 nm and 1401 nm , which can be used as reference

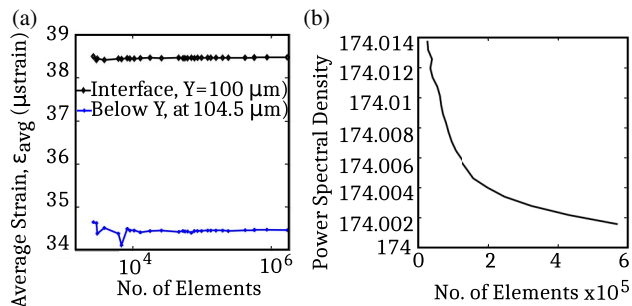


Fig. 2. FE mesh convergence results for (a) a strain at two different depth-wise planes [shown in Fig. 7(a)] and (b) total spectral power density.

peaks for distributed strain sensing. Similar periodic transmission peaks are also observed on the longer wavelength (pass-band) side beyond 1566 nm . The bandgap has a slight offset of 10 nm compared to the theoretical estimate owing to the geometry of the waveguide. The nature of wavelength specific propagation in the passband and stop band due to the underformed structure is shown in Fig. 4. The total grating length ($L_g = 40 \mu\text{m}$) can be longer than $12 \mu\text{m}$ [grating order ($m = 6$) times pitch ($\Lambda = 2 \mu\text{m}$)]. Hence, the grating is long enough that it sufficiently allows the transmission field to develop uniformly along the length of the grating (close to periodic field assumption). Shortening of the grating would tend to

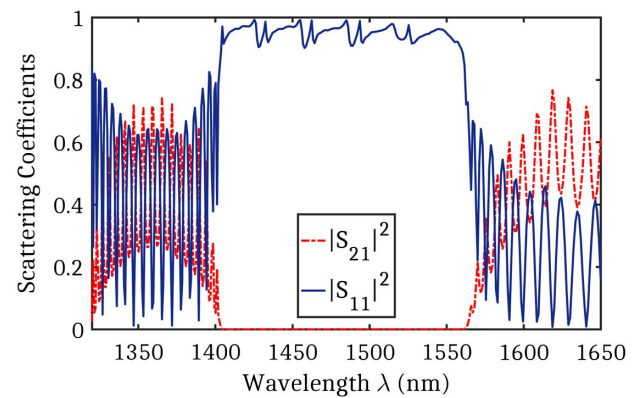


Fig. 3. Transmission and reflection characteristics shown in terms of S_{21} and S_{11} spectra, respectively.

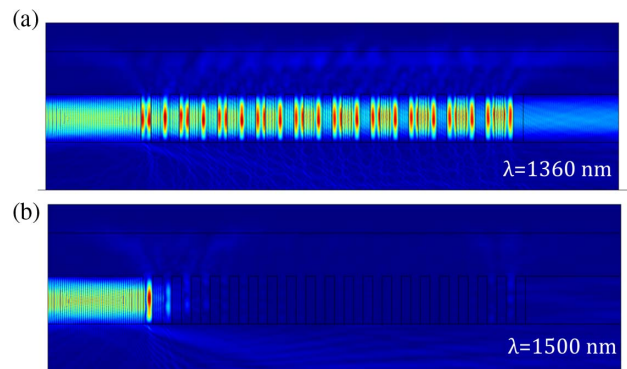


Fig. 4. Frequency domain wave field distribution (a) passband response for a wavelength of 1360 nm and (b) stop band response for a wavelength of 1500 nm .

alter the uniformity of the periodic field significantly and therefore is not recommended. The transmitted wave field through the grating shows a small and insignificant amount of leakage asymmetrically distributed on the upper region of air and the lower region of Si (Fig. 4). The primary transmitted field is localized at the mid-depth of the grating. The edge effect is unavoidable although it does not affect the downstream field along the grating. Hence, it is concluded that the depth chosen in the present simulation is sufficiently large compared to the edge effect polluting the transmission field intensity. If the depth is further reduced, the edge effect and leakage would be stronger and the transmitted field intensity will drop. However, from the fabrication point of view, creating a deep etch perfectly is difficult and a reduced depth will reduce the etching time, and in that case finer pitch can be made with smaller depth using electron beam lithography.

The transmission peaks are located at periodic intervals on the long wavelength side and similarly on the short wavelength side with reference to the transmission bandgap (Fig. 5). The peaks are periodically arranged according to the integral multiple of the pitch length scale parameters ($n_a d_a$ and $n_b d_b$). The number of prominent peaks on the envelopes on the long and short wavelength sides (passband regions) are limited due to the depth and width of the grating and its bulk dielectric properties. These envelopes will slightly broaden if the grating cross section is increased.

For the PC to be used as a strain sensor, the spectral peak shift at the bandgap edges is of interest to correlate with change in the strain. In our proposed scheme, we first select the prominent transmission peak (with transmission >70%) to the left of the bandgap as reference (Fig. 5). It is centered at 1371.82 nm with transmission of 72.83% power with a quality factor of 450.28. The integrated power density over wavelengths in the first passband is 1.98 W-nm. The behavior of the waveguide under longitudinal strain is discussed next.

A. Longitudinal Strain Sensing

Longitudinal load is applied at the right end boundary (of the cantilever) along the positive X direction, as shown in Fig. 6. Strain and displacement in the longitudinal direction are calculated for varying loads. In the grating section, the Si layers (vertical pillars) undergo a small amount of mostly rigid translation displacement due to the discontinuous composition of the grating. As a result, the air layer thickness changes due

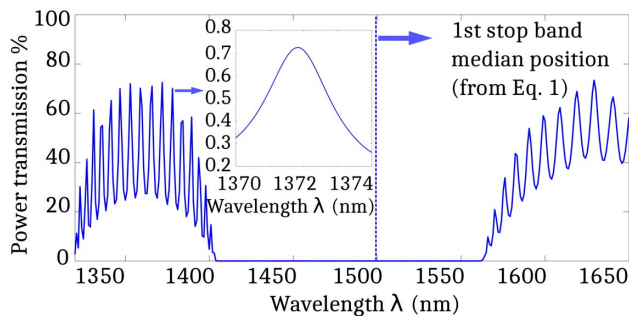


Fig. 5. Transmission spectra; inset shows first peak >70% power, wavelength $\lambda_0 = 1371.82$ nm. The FWHM of the resonance is 3.046 nm.

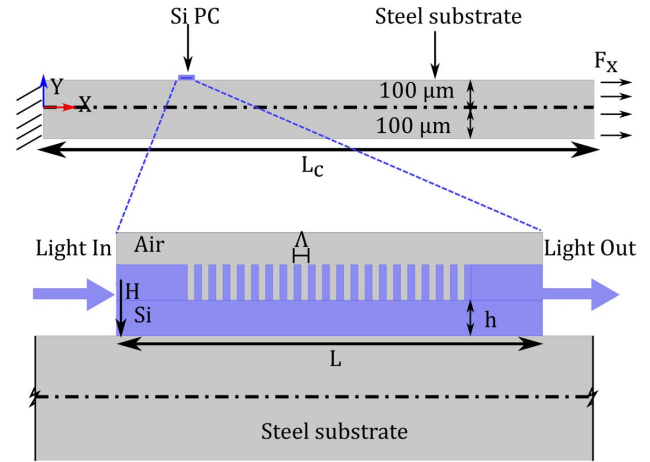


Fig. 6. Schematic representation of steel cantilever with silicon PC waveguide structure under longitudinal force F_x ($L = 60 \mu\text{m}$, $H = 10 \mu\text{m}$, $h = 5 \mu\text{m}$, $\Lambda = 2 \mu\text{m}$, $L_c = 6000 \mu\text{m}$).

to the displacement of adjacent Si layers. This change in the air layer thickness along the mid-depth of the grating height h is calculated and the deformation data is used for electromagnetic simulations to find the shift in the transmission spectral characteristics.

The sensing objective is to be able to measure the longitudinal strain generated on the surface of the host structure, where the PC is bonded and when a load is applied to the beam, from the correlated spectral peak(s) of interest. To obtain the most appropriate quantifiable strain correlation, longitudinal strains along three different depth-wise positions have been compared with that of the actual free surface strain on the cantilever at the grating location, without any Si PC waveguide structures bonded on it.

The three depth-wise lines are chosen as follows: strains at the waveguide–host interface (case B), bottom of the grating (case C), and top of the grating (case D), as shown in Fig. 7(a). Figure 7(a) shows a comparison of the longitudinal strain distribution for the three cases A–D. Strain along the line B is found to

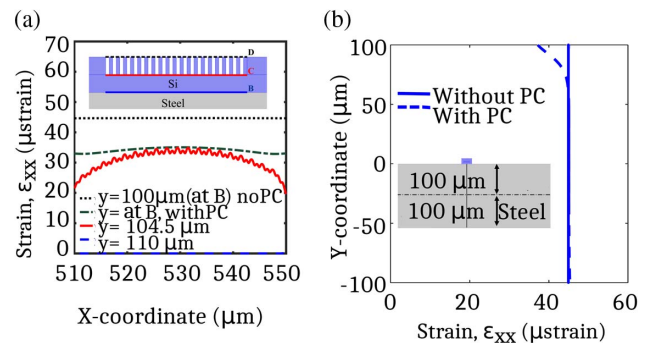


Fig. 7. (a) Longitudinal strain distribution at different positions. “A” indicates free surface without silicon layer. (b) Comparison of the longitudinal strain along a vertical line through mid-span cross section of PC with that of the free surface case. (Inset shows the steel substrate and the vertical line along which longitudinal strain is measured).

be in good match with that of the original free surface of the host structure and hence the mean value of the strain distribution at B is selected as the target measurand for sensing.

The longitudinal strain variation along a vertical line through the mid-span section of the PC is compared to the one without the PC (for the same load F_x) to find the significance of the grating interfaces with beam surface on the bending strain. It can be seen that when the PC is bonded on the surface, the target strain is fully recovered or developed at a depth $y = 60 \mu\text{m}$. The corresponding correction factor (shift in strain divided by reference strain) can be introduced for accurate prediction. However, this factor is dependent on the mismatch in the elastic properties of Si and substrate material. Separate calibration data would be needed to apply this to other material.

The frequency domain electric field transmission spectra through the PC for a peak at a wavelength of 1371.82 nm is shown in Fig. 8. The transmission characteristics of this peak with varying load is shown in Fig. 9. A redshift is observed with an increase in load.

The mean values of strain at depth B for varying longitudinal loads are shown against the shift in the transmission spectral peak of interest in Fig. 10(a). The fitted curve is linear, which is useful to convert the sensor output to into strain in a straightforward manner. Also, the actual strain on the free surface of the cantilever can be estimated considering the constant correlation factor, which is plotted in Fig. 10(b) as percent error in strain compared to free surface strain.

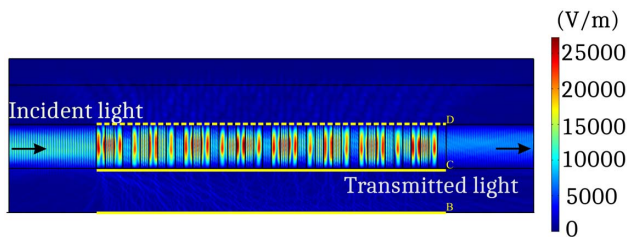


Fig. 8. Frequency domain electric field distribution in the PC, showing the transmission at the wavelength of 1371.82 nm under unstrained condition.

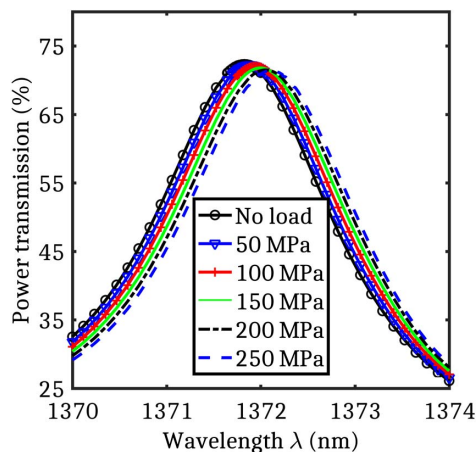


Fig. 9. Power transmission spectral peak of the PC for varying longitudinal loads.

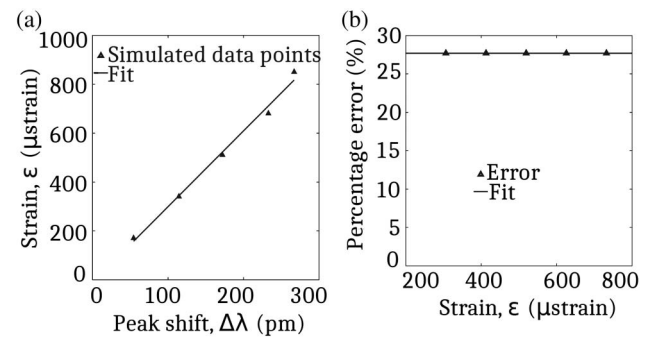


Fig. 10. (a) Wavelength shift versus mean strain along the Si-steel interface. (b) Percentage error in axial strain, when compared to the free surface case.

B. Flexural Strain Sensing

For flexural strain sensing evaluation, a transverse load is applied at the free end of the cantilever, as shown in Fig. 11. The transverse shear stress profile applied is given by

$$\tau_{xy} = \alpha y^2 + \beta, \quad (14)$$

where y is the thickness coordinate, and α and β are constants determined based on surface traction conditions. Shear stress is maximum (τ_{\max}) at $y = 0$ and vanishes at both surfaces ($y = \pm 100 \mu\text{m}$). The total load F_y distribution is determined accordingly on the edge. The sensing scheme is the same as discussed earlier for the longitudinal case.

Flexural strains along the three line segments at the three depth-wise positions [B, C, and D in Fig. 7(a)] are compared in Fig. 12 with that of the reference free surface condition (A). Small fluctuation in the strain profile at depth B is due to the grating layers. The mean value of strain at B for varying transverse loads is plotted against the shift in the wavelength of the spectral peak in Fig. 14. The fitted curve is a linear one which comes out to be a reasonable approximation of the calibration data and is practically useful.

Among the dominant spectral peaks in the transmission band edge, some spectral peaks show positive shift, while some others show negative shift in wavelength. Due to the transverse load, the grating bends. The peak shifts are dynamic due to alternate tension-compression cycle when the structure oscillates dynamically. Hence, a perfectly normal incidence of light will not occur in all the Si pillars, as shown in Fig. 13.

The angle of incidence keeps on reducing from the first pillar to the last pillar, which is due to the specific nature of the strain gradient. Due to this, the pattern of peak shift changes from peak to peak over the transmission band. All of the

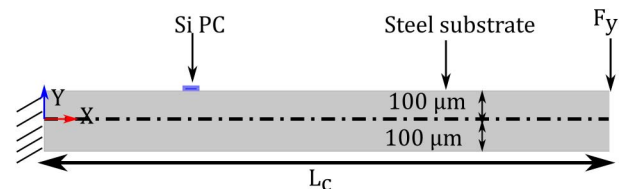


Fig. 11. Schematic showing the PC with host cantilever subjected to transverse load.

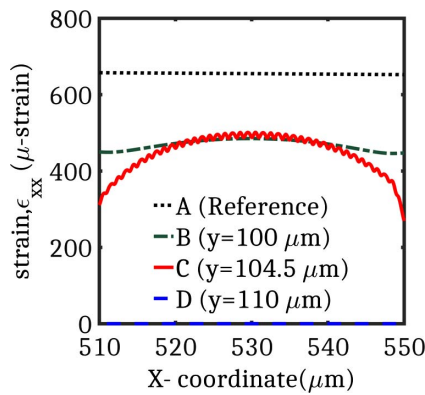


Fig. 12. Distribution of flexural strain (ϵ_{xx}) at various depth-wise locations, for the transverse load. $\tau_{\max} = 1$ MPa.

prominent peak shifts are shown in Fig. 16(b). As shown in Fig. 13, we have used until now the P1 peak shift for determining the mean strain over the sensor. In both the cases of longitudinal and flexural strains, the data shows some scatter [Figs. 10(a) and 14]. Under a dynamic loading, two factors would be additionally important—one is the temporal change in the positive and negative shifts in the peak due to compression and tension, and the other is the non-uniform localization of strain due to transient dynamic or wave-type loading. To improve the sensor calibration procedure for these conditions, we consider the response of multiple spectral peaks.

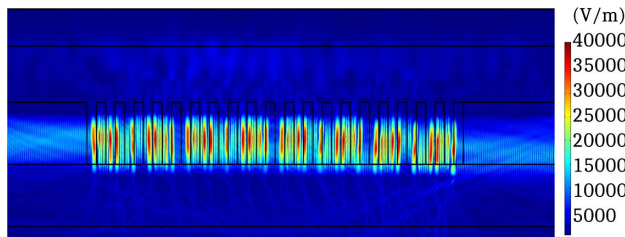


Fig. 13. Frequency domain distribution of electric field (E_y) under transverse load (175 N) for $\lambda = 1370.6$ nm (P1). The ideal normal incidence to the Si pillars is no longer preserved, which is due to the bending of the PC waveguide.

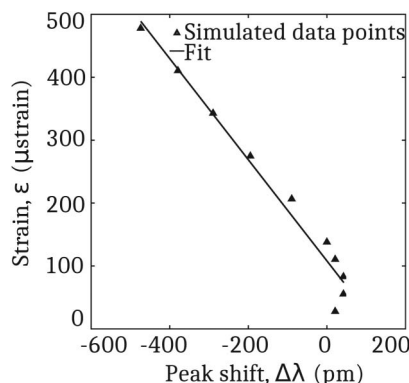


Fig. 14. Mean flexural strain versus peak wavelength shift for varying transverse loads of peak 1.

C. Multispectral Correlation

For multispectral peak correlation, the wide transmission spectrum of wavelengths ranging from 1370 nm to 1420 nm is utilized. In addition to the primary reference peak P1 at 1371.82 nm, five other peaks (P2–P6) with power levels more than 70% are considered. They are shown in Fig. 15 with their reference peaks at wavelength of 1365.61 nm, 1359.31 nm, 1353.07 nm, 1346.97 nm, and 1341.20 nm, respectively. Correlation of these peak shifts with strain are then estimated for varying longitudinal static loads, as shown in Fig. 16(a), indicating monotonic redshift.

For the same mean strain, we have obtained five different peak shifts using five independent spectral peaks. Thus, instead of using only a single peak shift and calibration factor, the objective is to express the strain as a linear function of six different peak shifts. This gives the advantage of minimizing the error in calibration factor for scatter in the calibration data and also for a time-dependent strain calculation or in spatial mapping of the strain distribution when such information concerning spatiotemporal variation is hidden inside all the different spectral peaks.

To establish this mapping, with specific application in transient dynamic sensing, we have developed a moving window recursive time series model for accurately sensing the strain.

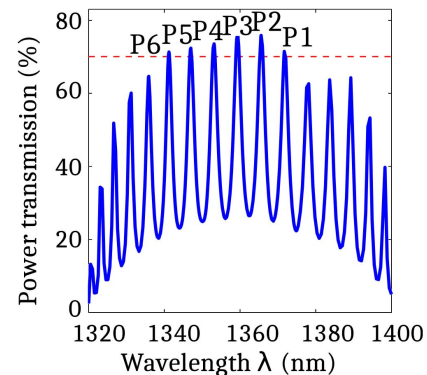


Fig. 15. Transmission peaks of the PC for unstrained case. The dotted red line indicates a transmitted power level of 70% of the maximum normalized power.

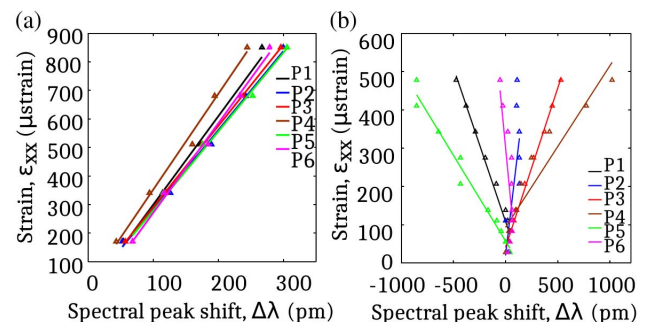


Fig. 16. Correlation of multispectral peak shifts for (a) longitudinal loads and (b) transverse loads; all are under static conditions.

D. Transient Strain Sensing

Experimental data from shock tunnel experiments [25] are used to validate the strain–peak shift correlation. The surface strain in the structure due to an aerodynamic shock loading is estimated. The acceleration of the test structure is measured and is converted to an equivalent dynamic force data using the force measurement technique. The test was carried out in the Hypersonic Shock Tunnel facility at IISc. A gaseous shock with Mach number of 5.75 was applied on the test structure by mounting it on a rubber bush attached to a longitudinal sting as support in the test section. The test structure was a blunt cone made of steel with three MEMS piezoelectric accelerometers inside the housing and attached to the rubber bush. The structure resembles the nose of a typical space re-entry vehicle. The accelerometer signals were used along with a mathematical correlation model of the test structure [25] to arrive at the force time history experienced by the test structure. The physical origin of the force is the high-speed aerodynamics-induced stagnation and drag force on the blunt nose cone. In the present study, we rescale the force and convert it into a strain time history assuming the photonic crystal sensor as the proposed new sensor placed on the longitudinal central sting. This type of highly transient strain measurement would be a potential application with advantages in terms of sensitivity and response time as compared to the standard accelerometers. The full sampling rate for the shock tunnel data was at 1 MHz while the accelerometer bandwidth was restricted to 10 kHz. The response time for the primary shock incidence on the test structure was about 500 μ s.

The primary shock which exists for about 500 μ s has a very high frequency noise, which is removed using a low-pass filter. This gives us representative force data (see Fig. 17). This force time history is then used as the input for time-dependent strain analysis under longitudinal loading on the cantilever structure (calibration sample). The spatial strain at the PC waveguide location is calculated for the entire time span using a moving time window based regression, which is discussed in the next section.

The simulated strain time history provides the reference data for validating the developed scheme of strain sensing. The time span is divided into several time windows, each containing six strain data points since we use six spectral peaks.

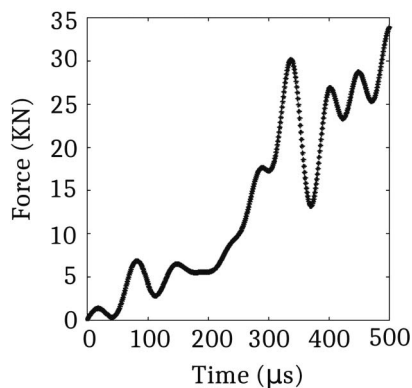


Fig. 17. Experimental force time history due to primary shock wave impact on a test specimen, which is applied for dynamic strain sensing analysis.

This contributes to the vector of strain data $\{\varepsilon_i\}$, where the strain can be expressed as a linear combination of multispectral peak shifts as

$$\begin{bmatrix} \varepsilon_{xx}(t_1) \\ \varepsilon_{xx}(t_2) \\ \varepsilon_{xx}(t_3) \\ \varepsilon_{xx}(t_4) \\ \varepsilon_{xx}(t_5) \\ \varepsilon_{xx}(t_6) \end{bmatrix} = \begin{bmatrix} \Delta\lambda_1^{(P_1)} & \Delta\lambda_1^{(P_2)} & \Delta\lambda_1^{(P_3)} & \Delta\lambda_1^{(P_4)} & \Delta\lambda_1^{(P_5)} & \Delta\lambda_1^{(P_6)} \\ \Delta\lambda_2^{(P_1)} & \Delta\lambda_2^{(P_2)} & \Delta\lambda_2^{(P_3)} & \Delta\lambda_2^{(P_4)} & \Delta\lambda_2^{(P_5)} & \Delta\lambda_2^{(P_6)} \\ \Delta\lambda_3^{(P_1)} & \Delta\lambda_3^{(P_2)} & \Delta\lambda_3^{(P_3)} & \Delta\lambda_3^{(P_4)} & \Delta\lambda_3^{(P_5)} & \Delta\lambda_3^{(P_6)} \\ \Delta\lambda_4^{(P_1)} & \Delta\lambda_4^{(P_2)} & \Delta\lambda_4^{(P_3)} & \Delta\lambda_4^{(P_4)} & \Delta\lambda_4^{(P_5)} & \Delta\lambda_4^{(P_6)} \\ \Delta\lambda_5^{(P_1)} & \Delta\lambda_5^{(P_2)} & \Delta\lambda_5^{(P_3)} & \Delta\lambda_5^{(P_4)} & \Delta\lambda_5^{(P_5)} & \Delta\lambda_5^{(P_6)} \\ \Delta\lambda_6^{(P_1)} & \Delta\lambda_6^{(P_2)} & \Delta\lambda_6^{(P_3)} & \Delta\lambda_6^{(P_4)} & \Delta\lambda_6^{(P_5)} & \Delta\lambda_6^{(P_6)} \end{bmatrix} \times \begin{bmatrix} a^{(P_1)} \\ a^{(P_2)} \\ a^{(P_3)} \\ a^{(P_4)} \\ a^{(P_5)} \\ a^{(P_6)} \end{bmatrix}, \quad (15)$$

where $\Delta\lambda_i$ is the peak shift for strain at time i and P_j denotes the spectral peak j for which the shift is calculated. The procedure to find the coefficients $a^{(P_1)}$ to $a^{(P_6)}$ is as follows. We take six strain data point values over a time window. For each peak, we calculate the peak shifts from the static response simulation [see Section 3.C, Fig. 16(a)]. We have six spectral peaks forming the six columns of the 6×6 matrix $[\Delta\lambda_j^{(P)}]$. We solve the linear system shown in Eq. (15). We get the six coefficients from a minimum-norm solution ($x = A^{-1}b$). The regression parameters $a^{(P_1)}$ to $a^{(P_6)}$ are estimated in the present example as

$$\{a^{(P_j)}\}^T = [-1.1669 \quad 2.3257 \quad 0 \quad -0.4108 \quad 1.4457 \quad 0.4437]^T. \quad (16)$$

Next, we fit $\Delta\lambda_i$ against six dynamic strain data points $\varepsilon_i(t_i)$ for each peak in a moving window. Note that we used six spectral peaks above 70% power level. More number of peaks with lower power level may be considered and the dimension of the matrix and vectors in Eq. (15) needs to be increased accordingly to make the parameter estimation problem well posed. This

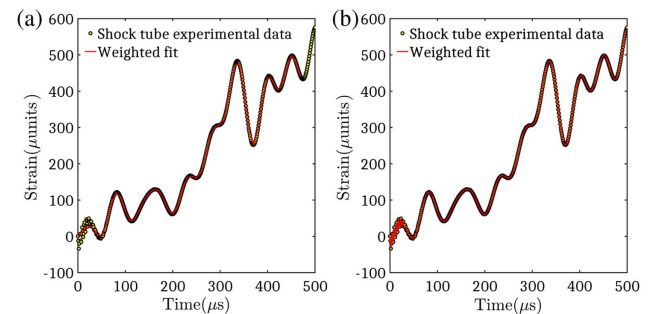


Fig. 18. Dynamic strain estimated with sampling rates of (a) $1/(10\Delta t)$ and (b) full sampling rate ($1/\Delta t$) using six spectral peak shift calibration data under static loading ($\Delta t = 1 \mu$ s).

should improve the sensitivity of the sensor at the expense of more intensive calculation, although the spectral peaks having lower power level are expected to introduce higher noise-to-signal ratio in a practical application while considering the additional factors of coupling the light path to the grating structure. Two different sampling rates $1/(10\Delta t)$ and $1/(\Delta t)$ are used to estimate sampled strains from the loading history and the resulting accuracy while predicting the original transients in the time history (Fig. 18). These reconstructed signals show that the strain transients are accurately predicted except a small amount of errors in the initial time.

4. CONCLUSION

A quasi-one-dimensional photonic crystal waveguide of silicon integrated with the host structure has been considered for distributed strain sensing scheme development. A wide stop band ranging from 1401 nm to 1566 nm is designed with the band edge spectral peak shift for sensing strain. The observed reference peak adjacent to the stop band edge of transmission spectra has a maximum transmission of 72.83%, Q -factor of 450.28, and full width at half-maximum (FWHM) of 3.046 nm. Static strain sensing characteristics of the sensor are studied by applying a range of loads on the host structure producing the shifts in the spectral peaks in the wavelength range of 1350–1360 nm. It shows a redshift due to both longitudinal and transverse strains of tensile nature. Dynamic characteristics are analyzed by applying shock loading. Dynamic localization of the strain field along the grating length is observed. The temporal and resulting spatial distribution effect in the strain fields at different time instants are captured in the proposed calibration method using a linear recursive model involving multispectral peak shifts. The maximum sensitivity of the sensor is obtained as 4.029 pm/ μ strain by taking advantage of the multipoint calibration, whereas a single first peak gives a sensitivity of 0.36 pm/ μ strain. The proposed sensing scheme can be used for transient dynamic sensing in load monitoring or structural health monitoring where high fidelity data with coarse measurement would be advantageous over a conventional fiber Bragg sensor.

Funding. AR&DB ACECOST Centre, Department of Aerospace Engineering; Indian Institute of Science.

Acknowledgment. Authors acknowledge the use of the computational facility at the AR&DB ACECOST Centre, Department of Aerospace Engineering, IISc to carry out the simulation work, and the shock tunnel facility at the LHSR, Department of Aerospace Engineering, IISc for the shock wave experimental data.

REFERENCES

- Y. J. Rao, "Recent progress in applications of in-fiber Bragg grating sensors," *Opt. Lasers Eng.* **31**, 297–324 (1999).
- C.-C. Ma and C.-W. Wang, "Transient strain measurements of a suspended cable under impact loadings using fiber Bragg grating sensors," *IEEE Sens. J.* **9**, 1998–2007 (2009).
- H.-Y. Ling, K.-T. Lau, W. Jin, and K.-C. Chan, "Characterisation of dynamic strain measurement using reflection spectrum from a fiber Bragg grating," *Opt. Commun.* **270**, 25–30 (2007).
- K.-C. Chuang, H.-T. Liao, and C.-C. Ma, "Dynamic sensing performance of a point-wise fiber Bragg grating displacement measurement system integrated in an active structural control system," *Sensors (Basel)* **11**, 11605–11628 (2011).
- G. C. Kahandawa, J. Epaarachchi, H. Wang, and K. T. Lau, "Use of FBG sensors for SHM in aerospace structures," *Photon. Sens.* **2**, 203–214 (2012).
- H. C. Yuan, J. Shin, G. Qin, L. Sun, P. Bhattacharya, M. G. Lagally, G. K. Celler, and Z. Ma, "Flexible photodetectors on plastic substrates by use of printing transferred single-crystal germanium membranes," *Appl. Phys. Lett.* **94**, 013102 (2009).
- I. McKenzie and N. Karafolas, "Fiber optic sensing in space structures: the experience of the European Space Agency," *Proc. SPIE* **5855**, 262–269 (2005).
- C.-C. Ma, Y.-H. Huang, and S.-Y. Pan, "Investigation of the transient behavior of a cantilever beam using PVDF sensors," *Sensors* **12**, 2088–2117 (2012).
- A. Jain, S. J. Kumar, D. R. Mahapatra, and V. T. Rathod, "Development of P(VDF-TrFE) films and its quasi-static and dynamic strain response," *Int. J. Eng. Res. Technol.* **2**, 2598–2605 (2013).
- A. Jain, S. J. Kumar, S. Srikanth, V. T. Rathod, and D. Roy Mahapatra, "Sensitivity of polyvinylidene fluoride films to mechanical vibration modes and impact after optimizing stretching conditions," *Polym. Sci. Eng.* **53**, 707–715 (2012).
- T. M. Benson, S. V. Boriskina, P. Sewell, A. Vukovic, S. C. Greedy, and A. I. Nosich, "Micro-optical resonators for microlasers and integrated optoelectronics," in *Frontiers of Planar Lightwave Circuit Technology* (Springer, 2006), Vol. **216**, pp. 39–70.
- M. Agresti, P. Charles, R. Paoletti, and M. Vallone, "Wavelength-selective distributed Bragg reflector device," *European patent EP 1391756 A1* (25 February, 2004).
- P. Prabhathan, V. M. Murukeshan, Z. Jing, and P. V. Ramana, "Broadband tunable bandpass filters using phase shifted vertical side wall grating in a submicrometer silicon-on-insulator waveguide," *Appl. Opt.* **48**, 5598–5603 (2009).
- A. S. Jugessur, J. Dou, J. S. Aitchison, R. M. De La Rue, and M. Gnan, "A photonic nano-Bragg grating device integrated with micro fluidic channels for bio-sensing applications," *Microelectron. Eng.* **86**, 1488–1490 (2009).
- W. Streifer, D. Scifres, and R. Burnham, "Coupled wave analysis of DFB and DBR lasers," *IEEE J. Quantum Electron.* **13**, 134–141 (1977).
- T. Utaka, K. Tamaki, H. Takase, and T. Ukachi, "Optical waveguides fabricated by using all-wet-photolithography technique with UV curable sol-gel materials," in *Optical Fiber Communication Conference and Exhibit* (2002), pp. 678–679.
- J. Ctyroky, S. Helfert, R. Pregla, P. Beinstman, R. Baets, R. Deridder, R. Stoffer, G. Klaasse, J. Petracek, P. Lalanne, J. P. Hugonin, and R. M. Delarue, "Bragg waveguide grating as a 1D photonic band gap structure: COST 268 modeling task," *Opt. Quantum Electron.* **34**, 455–470 (2002).
- J. D. Joannopoulos, S. G. Johnson, J. N. Winn, and R. D. Meade, *Photonic Crystals: Molding the Flow of Light*, 2nd ed. (Princeton University, 2008).
- D. B. Davidson, *Computational Electromagnetics for RF and Microwave Engineering* (Cambridge University, 2005).
- Comsol Multiphysics v. 5.0., www.comsol.com.
- M. A. Hopcroft, W. D. Nix, and T. W. Kenny, "What is the Young's modulus of silicon?" *J. Microelectromech. Syst.* **19**, 229–238 (2010).
- P. Djemia and K. H. Bouamama, "Ab-initio calculations of the photo-elastic constants of the cubic SiC polytype," *J. Phys. Conf. Ser.* **454**, 012060 (2012).
- P. T. Rakich, P. Davids, and Z. Wang, "Tailoring optical forces in waveguides through radiation pressure and electrostrictive forces," *Opt. Express* **18**, 14439–14453 (2010).
- A. Feldman, "Relations between electrostriction and the stress-optical effect," *Phys. Rev. B* **11**, 5112–5114 (1975).
- N. Sahoo, D. R. Mahapatra, G. Jagadeesh, S. Gopalakrishnan, and K. P. J. Reddy, "An accelerometer balance system for measurement of aerodynamic force coefficients over blunt bodies in a hypersonic shock tunnel," *Meas. Sci. Technol.* **14**, 260–272 (2003).